INTERFACIAL MIXING OF DENSE-WATER OVERFLOW IN A CONVERGING AND UP-SLOPING CHANNEL

Janek Laanearu[1], Alan J S Cuthbertson[2], & Peter A Davies[3]

[1]Department of Mechanics, Tallinn University of Technology, Estonia, Tallinn 19086
[2]School of Built Environment, Heriot-Watt University, UK, Edinburgh EH14 4AS
[3]School of Engineering, Physics and Mathematics, University of Dundee, UK, Dundee DD1 4HN

E-mail: janek.laanearu@ttu.ee

Abstract

Purpose of the study is to explain experimental results of dense bottom currents in the upward-sloping, converging triangular channel. High-resolution velocity and density profiles are used to analyze the changes of interface shape and mixing process for different salt-water inflow rates and bottom slopes. The stratified flow dynamics of the convectively accelerating dense water overflow is determined with an upward cascading process of energy toward the upper fresh-water layer. The internal-flow structure reveals different interfacial processes for two bottom slope cases (denoted as *Weir* and *Sill*). In the case of relatively steep up-sloping converging-channel and horizontal exit-channel (*Weir*) sections, the deep-water motion has sub-critical conditions throughout and is characterized by a comparatively sharp density interface and relatively small deep-water velocities. In the case of relatively mild up-sloping channel and highest bottom point (*Sill*) between converging-channel and exit-channel sections, the internal motion is determined by relatively large deep-water velocities and diffused density interface near to the ″sill″ section. The density and velocity interfaces are vertically diverged in the case of combined Froude number sq $\boldsymbol{G}^2 \rightarrow 1$. The density-profile gradient minimum in the *Weir* case is determined by the density excess $\rho' \sim 0.5$ and in the *Sill* case by $\rho' \sim 0.3$ for the flow rates considered. The internal-energy function is used to determine the internal-head losses due to bottom friction. The gradient Richardson number profiles are calculated to characterize the stationary turbulent process in the topographically constrained and stratified flow cases. The relationship between the interfacial Reynolds stresses and the net-entrainment process is discussed.

Introduction

The motivation for the study is the topographic control that is known to affect buoyancy-driven exchange processes in natural channels and basins such as fjords and estuaries. In the case of fjord dynamics, the essential elements of this control are the converging lateral and ocean bed topography approaching the sill at the entrance to the fjord. There are, however, some uncertainties in quantifying the effects due to bottom stress and internal mixing on the topographically-constrained, deep-water flow. The freshwater runoff and associated salt wedge dynamics responsible for the exchange involves strong gradients of velocity and density (Csanady, 1984; Sargent & Jirka, 1987; Arita & Jirka, 1987ab; *etc*). The deep layer of reduced gravity and inviscid current entering into the channel from an upstream basin becomes hydraulically-controlled at a sill located in the channel. However, the effect of friction is to change the critical-flow conditions. Results from scaled experiments carried out in an idealized, converging channel topography installed in NTNU *Coriolis Rotating Basin* (Trondheim, Norway), are compared with theoretical model predictions for inviscid (Rotating hydraulics) and frictional (Ekman model) approaches in Cuthbertson *et al*. (2011).

A series of laboratory experiments were conducted within a submerged and convergent vee-shaped channel to investigate internal flow dynamics for dense-water flow over obstacles in relatively steep and mild up-sloping beds, in both rotating and non-rotating cases. Only non-rotating cases are considered here. High-resolution velocity and density profile measurements have been used to determine the location and form of the interfaces formed by the generated dense bottom gravity currents and the overlying, quiescent receiving waters. One of the purposes of this study is to describe how frictional boundaries and interfacial mixing are related to the dynamics of dense-water flow in non-rectangular and -rotating channel (Laanearu *et al.*, 2011b). The interface longitudinal profiles of the gradually-varied flow in the reduced-gravity limit are due to changes of non-rectangular channel geometry, bottom friction and interfacial processes. Laanearu and Davies (2007) formulated a model for stratified, internal flows of this type for use in natural channels and introduced the concept of quadratic-section channels. In such channels,

the flow has one width maximum at the surface and a single depth maximum (located in this study at the centre line of cross section); the flow cross-sectional shapes are then classified quantitatively by the value of the parameter $\xi \geq 1$, representing the ratio of the bank-full area to the cross-sectional area of flow. In the study by Laanearu *et al.* (2011a) it is demonstrated how internal hydraulic theory for such channels ($\xi = 1.8$ *i.e.* the cross-sectional area of flow is smaller than the parabolic cross section and is large than the triangular cross section), including internal head loss, can be used to predict the stratified bi-directional fluxes and density-interface depths observed in a river mouth of the Baltic Sea.

The laboratory system utilized for the non-rectangular and -rotating channel deep-water overflow experiments is described herein, along with the instrumentation used for density and velocity measurements. The qualitative description of measured stratified flow structure is then given for both bed slope conditions tested, while quantitative characteristics of velocity and density profile measurements near to the ″sill″ section are analyzed in both cases. An internal-energy function for deep-water flow in a triangular channel is introduced to analyze the internal dissipation due to bottom friction. Finally, gradient Richardson number profiles are then calculated and their relationship with interfacial mixing processes is discussed.

Experimental system

The up-sloping triangular cross-sectional shape channel is sketched in Figure 1.

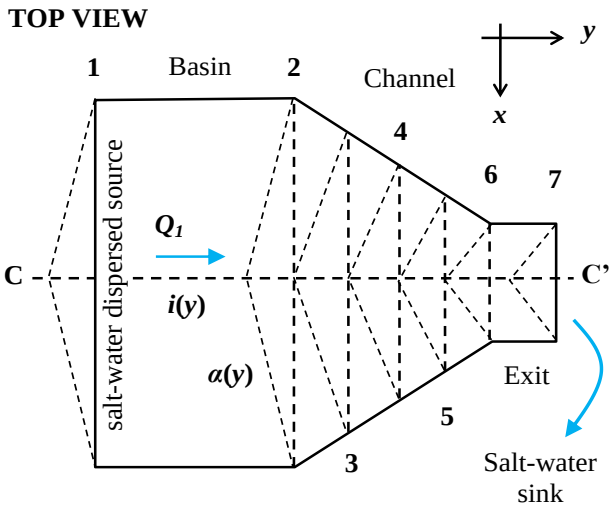

Figure 1: Schematic plan (*xy*-plane) of the topographic system consisting of basin, converging-channel and exit-channel sections. The longitudinal bottom slope $i(y)$ and the cross-sectional side slope $\alpha(y)$ vary in the direction of *y*-axis between the cross sections 1 - 7. Salt-water, with flow rate Q_1, circulation is shown by arrows between uniformly dispersed source (1) and point sink (near 7).

The Cartesian coordinate frame (*x*, *y*, *z*) is orientated with *x*- and *y*-axis in the cross- and along-channel directions, respectively, and the *z*-axis is anti-parallel to the gravitational acceleration vector $\mathbf{g} = (0,0, -g)$. The overall length of the basin, converging-channel section and exit-channel section is 3.5 m in the direction of the outflow along the CC'-axis (1.5 m, 1.5 m and 0.5 m long, respectively). The cross-sectional maximum width varies from 2.5 m in the basin (between cross sections 1 and 2, Figure 1) to 0.8 m at the channel exit section (between cross sections 6 and 7, Figure 1). The overall channel configuration is symmetric along the CC'-axis, while the converging, vee-shaped channel has variable cross-sectional side slope $\alpha(y)$ and longitudinal bed slope $i(y)$. Experiments were conducted with two different adverse longitudinal bed slopes $i_{cp} = -0.0663$ (*Weir*) and $i_{cp} = -0.0297$ (*Sill*) along the converging-channel section, (*i.e.* between cross sections 2 and 6, Figure 1). The exit-channel section was horizontal in the steep up-sloping channel case (like in V-notch weir). For the *Sill* case (i.e. mild up-sloping, converging channel) the maximum bed elevation occurred at section 6, with the exit channel section sloping downwards with $i_{ep} = 0.0270$.

The basin and converging-channel topography was installed within a 5 m diameter and 0.5 m deep circular tank. Prior to each experimental run, this circular tank was filled with freshwater ($\rho_0 = 998.5$ kg.m^{-3}) to a total tank-water depth of 0.44 m, submerging the converging-channel topography to a maximum in-topography water depth of $H_{max} = 0.334$ m for both up-sloping channel cases. With the lowest in-channel bed elevation defined as the reference $z_{min} = 0$, the channel-end elevation (cross section 6, Figure 1) was $z_{cs6} = 0.114$ m and $z_{cs6} = 0.0535$ m for steep and mild upward sloping channels, respectively. At the start of each experiment, brine solutions with density $\rho_1 = \rho_0 + \Delta\rho = 1011.4$ kg.m^{-3} and an initial volume flux $Q_1 = 0.3$ l.s^{-1} were pumped into the upstream basin via a dispersed source device (see Figure 1). During full experimental runs (with same bed slop), Q_1 values were increased incrementally ($0.3 \rightarrow 0.6 \rightarrow 0.9$) l.s^{-1}. The corresponding reduced gravity $g' = g(1 - r)$, with $r = \rho_0/\rho_1$, for this inflow was around $g' = 0.125$ m.s^{-2}. During each experimental run, the flow-rate Q_1 values were increased incrementally at prescribed times, allowing the bottom current reveal steady-state structure for each of the flow rate. The saline water layer was fully contained within the submerged, converging channel topography along its full length, before flowing along the uniform-width exit channel (between cross sections 6 and 7, Figure 1) and spilling out freely. The dense-water overflow was then routed to the right down via an inclined plate to the bottom of the circular tank, from where it was removed by a siphoned-sump device (see salt-water

circulation arrows in Figure 1). The above topographic system made possible the generation of bottom gravity currents in the two different bottom slope cases.

Instrumentation

At fixed locations, quasi-instantaneous density profiles $\rho(z)$ in the basin and converging-channel sections were taken by an array of high-resolution micro-conductivity probes. The probes were mounted on rigid support frames, each with a motorized rack system that allowed simultaneous and rapid profiling of the density field (Cuthbertson *et al.*, 2004) with an interval period of 10 seconds. During full experimental runs, Q_1 values were increased incrementally and a total of 3×100 density profiles were taken to measure the structure for each discharge value. In the case of steep upward-sloping channel, the density profiles were measured at three locations (x = –10, 0, 10 cm) near cross section 4 (Figure 1) and three locations (x = –5, 0, 5 cm) near cross section 6, with reference at the CC'-axis. In the case of mild upward sloping channel, the density profiles were measured along the CC'-axis, between cross sections 1 and 6 in Figure 1 at seven locations (y = –6.5, –21.5, –36.5, –56.5, –76.5, –178.5, –190.5 cm), with reference at cross section 6 position (for a photo of the lab system see Figure 2).

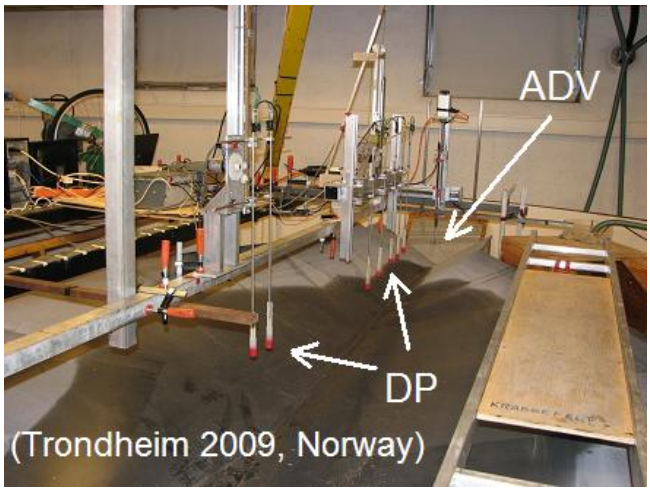

Figure 2: Mild upward-sloping vee-shape channel (*Sill* case) topography and instrumentation: 1) density probes (DP) and 2) acoustic Doppler velocimeter (ADV). (See also Figure 1 for the cross sections 1 - 7 locations.)

Three-component (u, v, w) velocity measurements were obtained using a Nortek AS Vectrino acoustic Doppler current profiler (ADV). The ADV probe was set to a measurement frequency of 10 Hz, with a vertical spatial resolution of 0.5 mm (corresponding to the constant vertical velocity 5 mm.s^{-1}). The velocity profiles were measured at five cross-channel locations (x = –10, –5, 0, 5, 10 cm), with x-axis reference fixed by CC'-axis (see Figure 1). The ADV section was positioned 5 cm downstream from the cross section 6 in Figure 1. In Figure 2, the topographic system and the instrumentation are presented. The ADV measurements were provided shortly after the DP profiling.

Measurements

High-resolution density and velocity profiles were measured to observe the overall appearance of stratified flow in two bottom slope cases (*Weir* and *Sill*). In the case of relatively steep up-sloping channel and horizontal exit-channel bottom (*Weir*), the deep-water motion is characterized by a comparatively sharp density interface and relatively small deep-water velocities. The flow in the case of relatively mild up-sloping channel and highest bottom point (*Sill*) between converging- and exit-channel sections is determined by relatively large deep-water velocities and diffused density interface near to the "sill" section. A time lag of 100×10 s between different source conditions was used, to separate the intensive density profiling of individual turbulent internal process adjusting to steady-state conditions. Mean density profiles from probes DP2 (near to cross section 4, Figure 1) and DP7 (near to cross section 6, Figure 1) are used to describe the longitudinal density transect in the *Weir* case. The y-coordinate positions of DP2 and DP7 are y = –0.75 m and y = –0.023 m, respectively. In the *Sill* case, the mean density profiles from probes DP8 (near to cross section 2, Figure 1), DP1 (near to cross section 4, Figure 1), DP4 (near to cross section 5, Figure 1) and DP6 (near to cross section 6, Figure 1) are used to describe the longitudinal density transect. The y-coordinate positions of the DP8, DP1, DP4 and DP6 are y = –1.785 m, y = –0.765 m, y = –0.365 m and y = –0.065 m, respectively. The channel Reynolds number ($\boldsymbol{Re_1}$), densimetric Froude number ($\boldsymbol{F_1}$) sq of the reduced gravity bottom current and the measured density-profile gradient minima ($d\rho/dz$) with *SI* units of kg.m^{-4} for source flow rate Q_1 with the units of l.s^{-1} are presented in Table 1. The ADV section inside the exit-channel section (in the vicinity of cross section 6, Figure 1) was employed to measure the velocity structure in different experimental runs shortly after the ending of density profiling procedure. In all runs the ADV section co-ordinate position was fixed to y = 0.05 m, with the reference in cross section 6 (Figure 1). The descending and ascending ADV probe excursions were only taken at certain section points and averaged to describe the vertical structure of velocity (see also Laanearu *et al.*, 2011b). The channel Reynolds number ($\boldsymbol{Re_1}$), densimetric Froude number ($\boldsymbol{F_1}$) sq of the reduced gravity bottom current and the measured velocity-profile gradient minima (dv/dz) with *SI* units of s^{-1} for source flow rate Q_1 with the units of l.s^{-1} are presented in Table 2. The measured high-resolution density profiles indicate that 1)

the pycnocline is squeezing toward the ″sill″ section in the *Weir* case and 2) the pycnocline is stretching in the same direction in the *Sill* case.

Table 1: Density profiles parameters.

Probe	Q_1	$\boldsymbol{Re_1}$	$\boldsymbol{F_1}^2$	$d\rho/dz$
DP 7	0.3	1198	0.4151	–1336
	0.6	1852	0.4575	–2105
	0.9	2356	0.4492	–2720
DP 2	0.3	408	0.0066	–690
	0.6	682	0.0108	–1233
	0.9	922	0.0144	–1866
DP 6	0.3	1339	0.7458	–470
	0.6	2009	0.7079	–538
	0.9	2565	0.7112	–529
DP 4	0.3	779	0.0979	–581
	0.6	1105	0.0702	–593
	0.9	1402	0.0685	–604
DP 1	0.3	505	0.0195	–655
	0.6	718	0.0141	–661
	0.9	929	0.0152	–668
DP 8	0.3	304	0.0032	–675
	0.6	461	0.0032	–677

Table 2: Velocity profiles parameters.

ADV	Q_1	$\boldsymbol{Re_1}$	$\boldsymbol{F_1}^2$	dv/dz
Weir	0.3	1237	0.4849	–1.5710
	0.6	1856	0.4603	–2.2193
	0.9	2402	0.4950	–3.6633
Sill	0.3	1458	1.1027	–3.2729
	0.6	2208	1.0947	–3.5843
	0.9	2849	1.1618	–5.7784

From the densimetric Froude numbers $\boldsymbol{F_1}$ sq, presented in Table 1 and Table 2, it can be concluded that the minimum velocity-profile gradient points almost coincide with the minimum density-profile gradient points in the *Weir* case. But the minima of density and velocity gradients are vertically diverged in the *Sill* case. It follows that the internal structure of dense bottom current near to the "sill" section (cross section 6, Figure 1) reveal different stratified flow structures in the different adverse-slope beds. In Figure 3, the combination of density excess profiles and velocity profiles, scaled by the approach velocity v_{core}, approximated from the mean profiles are shown for the steep (*Weir*) and mild (*Sill*) up-sloping channels, in the case of source flow rate Q_1 = 0.6 l.s^{-1}. In Figure 3(i) and 3(ii), the density excess $\rho' = (\rho(z)-\rho_0)/(\rho_0-\rho_1)$ = 0.5 interface height is $h_{50\%}$ = 0.0886 m for steep (*Weir*) and $h_{50\%}$ = 0.0751 m for mild (*Sill*) up-sloping beds, respectively. The dimensionless velocity v/v_{core} = 0.5 interface, between the bottom water (ρ' = 1) and overlying ambient water (ρ' = 0), is $h_{50\%}$ = 0.0890 m for steep (*Weir*) and $h_{50\%}$ = 0.0750 m for mild (*Sill*) adverse-slope beds, respectively. The critical deep-water height, defined for the vee-shape channel with side-slope angle of atan(α) = 33° and the inflow rate Q_1 = 0.6 l.s^{-1} is h_c = 0.0754 m. The measured interface heights suggests that the deep-water motion in the *Weir* and *Sill* cases are sub-critical inside of the basin and converging-channel sections, and only in the *Sill* case the dense-water flow reveal critical flow conditions near to the "sill" section (cross section 6, Figure 1).

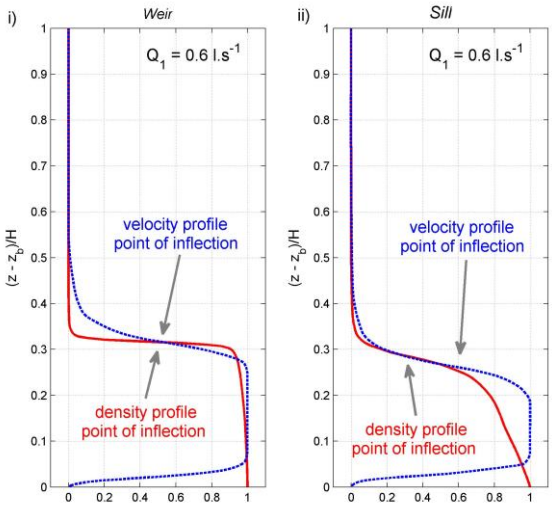

Figure 3: Combinations of the approximated density-excess ρ' (full curves) and scaled velocity v/v_{core} (dashed curves) profiles in i) *Weir* case and ii) *Sill* case. Density probes DP7 (*Weir*) and DP6 (*Sill*) data, and ADV data for *Weir* and *Sill* cases are used for the source flow rate Q_1 = 0.6 l.s^{-1}. ($H = z_s - z_b$ is local water depth at the *Thalweg*.)

Results presented in Figure 3(i) and 3(ii) also show that points of 50% excess density and 50% velocity co-inside well in both topographic cases. However, the dense bottom gravity current in the *Sill* case (Figure 3(ii)) reveals different internal structure, *i.e.* the minima of density-gradient ($d\rho/dz$) and velocity-gradient (dv/dz) diverge vertically. The density profile ″point-of-inflection″ representing the density interface corresponds in the *Sill* case roughly to the 30% excess density point (ρ' ~ 0.3), and the velocity gradient "point-of-inflection" that represents the velocity interface corresponds roughly to 60% point of velocity profile (v/v_{core} = 0.6). These gradient-type interfaces, representing the ″global″ minima of density- and velocity gradients, co-inside well in the *Weir* case. This observed situation is apparently related to the mixing conditions due to the strength of density stratification and the velocity shear between the moving dense water beneath ambient fresh-water body (see Davies, 2006). The buoyancy fluxes due to the net-entrainment process are

apparently important in the *Sill* case, when the bottom density current revealed the critical-flow conditions ($\boldsymbol{F_1} \rightarrow 1$) near ″sill″ section. The dense bottom current near ″sill″ section correspond to weak turbulent regime, because the channel Reynolds number $\boldsymbol{Re_1}$ was between 1200 and 2850.

Internal hydraulics

Following Laanearu and Davies (2007), the dimensionless internal-energy function, representing the lower- (B_1) and upper-layer (B_0) Bernoulli functions difference ($K_i = (B_1 - B_0)/g'$) for the small vertical density jump ($1 - r$) << 1 and the vee-shape channel geometry is given by:

$$K_i^* = 4\,K_{ii}^* \left(\left(\frac{1}{h_1^*} \right)^4 - \frac{q^2}{\left(\left(H^* \right)^2 - \left(h_1^* \right)^2 \right)^2} \right) + h_1^* + z_b^* \qquad (1)$$

where dimensionless parameters used are internal head $K_i^* = K_i/H_{max}$, volume flux parameter (corresponding here to lower layer flux) $K_{ii}^* = Q_1^2 \alpha^2 / \left(8 g' H_{max}^5 \right)$, local water depth $H^* = H/H_{max}$, lower layer height $h_1^* = h_1/H_{max}$ and bottom height $z_b^* = z_b/H_{max}$. The local water height is $H = h_0 + h_1$, where h_0 is upper layer thickness. The ratio of upper and lower layer fluxes is conveniently represented by the parameter q = abs(Q_0/Q_1). The solutions of Equation (1) can be parameterized by the combined Froude number sq $\boldsymbol{G}^2 = \boldsymbol{F_0}^2 + \boldsymbol{F_1}^2$ (cf Armi, 1986), where the densimetric Froude numbers sq of the upper and lower layers, respectively, are $F_0^2 = 2 v_0^2 h_1 / \left(g' \left(H^2 - h_1^2 \right) \right)$ and $F_1^2 = 2 v_1^2 / \left(g' h \right)$. In the first approximation, the dense bottom gravity current with the more-or-less quiescent ($v_0 \rightarrow 0$) upper layer situation is given by ($\boldsymbol{F_0} \rightarrow 0$ & $\boldsymbol{G}^2 \approx \boldsymbol{F_1}^2$). This simplified case is examined here to determine the bottom friction. Equation (1) can be used to define the internal-head loss parameter $\Delta E_I^* = K_{i(cs2)}^* - K_{i(cs6)}^*$ (cf Zhu & Lawrence, 2000; Cuthbertson *et al*., 2006; Laanearu *et al*., 2011b), representing the difference of the internal head ($K_{i(cs2)}^*$) at cross section 2 in Figure 1 and the internal head ($K_{i(cs6)}^*$) at cross section 6 in Figure 1.

The frictional effects due rigid bottom of idealized bed topography can be determined by the standard friction-factor formula, corresponding to weak turbulent regime. A converging-channel section of triangular (vee-shaped) cross-section was constructed from several laminated-surface plywood plates. The bottom surface was very smooth, and as a good approximation the empirical Blasius equation can be used to estimate the Darcy-Weishbach wall friction factor:

$$f = 0.3164 / \sqrt[4]{4\,\mathrm{Re}_1} \qquad (2)$$

where $\boldsymbol{Re_1}$ is the channel Reynolds number for dense bottom gravity current. The dimensionless internal head ($K_{i(cs2)}^*$) specified at cross section 2 in Figure 1, the critical flow internal-head loss (ΔE_I^*) using Blasius solution (2) and the combined Froude number sq $\boldsymbol{G}^2$ for the source flow rate Q_1 are presented in Table 3. The estimated combined Froude numbers, where the local stratification conditions due to velocity profile and reduced gravity are considered, indicate that the dense bottom gravity current tends to be internally controlled ($\boldsymbol{G}^2 \rightarrow 1$) in the mild up-sloping channel (*Sill* case). In the steep up-sloping channel (*Weir* case) only sub-critical conditions are determined near ″sill″ section, cross section 6 in Figure 1.

Table 3: Internal flow parameters.

	Q_1	$K_{i(cs2)}^*$	ΔE_I^*	$\boldsymbol{G}^2$
Weir	0.3	5.5554×10^{-1}	5.0557×10^{-4}	0.3057
	0.6	6.2385×10^{-1}	5.3196×10^{-4}	0.3380
	0.9	6.7352×10^{-1}	5.4054×10^{-4}	0.4111
Sill	0.3	3.7486×10^{-1}	9.5891×10^{-4}	0.7104
	0.6	4.4321×10^{-1}	1.0261×10^{-3}	0.8849
	0.9	4.9287×10^{-1}	1.0309×10^{-3}	0.9866

Interfacial processes

The measured pycnocline revealed different longitudinal internal structures for the *Weir* and *Sill* cases. The cross-sectional structure of pycnocline was self-similar in all cases *i.e.* the pycnocline cross-sectional thickness was conserved for particular deep-water fluxes. Uniform cross-sectional vertical mixing was apparent also from the measured ADV section velocity profiles near cross section 6 in Figure 1. This situation is different from the rotating tank experiments to examine the dynamics of geostrophic bottom dense gravity currents, where the cross-channel pycnocline thickness changes considerably (Cuthbertson *et al*., 2011). The stability of the stationary turbulent stratified flow is determined by the combination of the strength of the density gradient (as quantified by the Brunt-Väisälä frequency) and velocity shear (Reynolds stresses). The gradient Richardson number is defined by

$$Ri_g = -\frac{g}{\rho_0} \left(\frac{d\rho}{dz} \right) \Big/ \left(\frac{dv}{dz} \right)^2 . \qquad (3)$$

The gradient Richardson number profiles represented by Equation (3), based on the mean density and velocity profiles for the case of salt-water flow rate Q_1 = 0.6 l.s^{-1}, between the bottom water (ρ' = 1) and overlying ambient water (ρ' = 0), are presented in Figure 4. The maximum $\boldsymbol{Ri_g}$ zone near the pycnocline with a strong drop-off on either side is clearly distinguishable from Figure 4(i). This is due to the situation that in the *Weir* case the dimensionless velocity shear near the interface between the salt- and fresh-water is comparatively smaller compared with the density excess change for the same vertical thickness Δz (see Figure 3(i)). (Δz may be the local vertical scale of the pycnocline). In Figure 4(ii) the minimum $\boldsymbol{Ri_g}$ zone at the pycnocline with a strong increase on either side is apparent.

The dimensionless velocity shear near interface between the salt- and fresh-water is comparatively large compared with the density excess change for the same vertical thickness Δz in the *Sill* case (see Figure 3(ii)). In spite of approximations introduced, mainly due to measurements locations of density and velocity profiles, the gradient Richardson number is in good agreement with the internal structure observed for two different adverse-slope beds, *i.e.* in the *Weir* case $(\boldsymbol{Ri_g})_{\max} > 0.25$ and in the *Sill* case $(\boldsymbol{Ri_g})_{\min} < 0.25$ in the interfacial zone. In the case of the gradient Richardson number $\boldsymbol{Ri_g}$ smaller than its critical value 0.25, the turbulence is strong enough to weaken stratification due to vertical buoyancy fluxes (Ivey & Imberger, 1991).

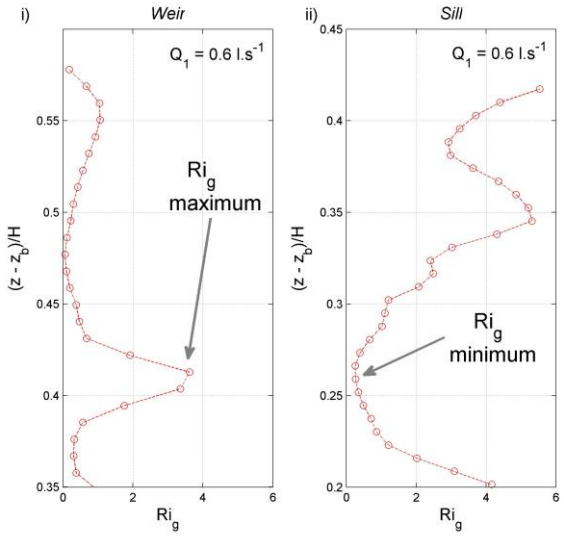

Figure 4: Gradient Richardson number profiles in i) *Weir* case and ii) *Sill* case. Salt-water source flux is $Q_1 = 0.6$ l.s^{-1}. ($H = z_s - z_b$ is local water depth at the *Thalweg*.)

Conclusions and discussion

The dense-water flow through the topographic system may be divided into three regions: the source region at the upstream end of the basin, the quasi-equilibrium region inside the basin and converging-channel sections and the sink region at the end of exit channel. The quasi-equilibrium region occupies comparatively large domain of the dense-water current. The main difference with the open-channel flow is due to presence of interface between dense- and fresh-water layers (Pratt & Whitehead, 2007). The flow inside of the basin and converging-channel section is determined by the ″internal-energy″ change per distance which is balanced by the loss due to bottom friction and dissipations due to interfacial processes. Apparently the net-entrainment processes made possible to speed up the dense bottom gravity current in the mild up-sloping bed (*Sill* case). The Reynolds stresses are reduced considerably in the zone of entrainment *i.e*. comparatively large vertical velocities (Sargent & Jirka, 1987). The laminarizing effect of the pycnocline was observed only together with relatively small deep-water velocities. The intensive mixing at pycnocline near the ″sill″ section was present in the case of relatively large bottom-water velocities. Non-rectangular channel stratified flow measurements data were analysed to present global properties of the velocity and density structures observed.

Acknowledgements

Financial support by Estonian Ministry of Education and Research (SF0140072s08) is appreciated. The study was initiated by the award to J L of a Distinguished Visiting Fellowship by the UK Royal Academy of Engineering. Experimental works in Trondheim 2009 (Norway) were supported by the EU HYDRALAB III Programme (Contract no. 022441).

References

Arita, M., & Jirka, G. H. (1987a, 113(10)). Two-layer model of saline wedge. I: Entrainment and interfacial friction. *ASCE J. Hydraul. Engng.*, pp. 1229-1248.

Arita, M., & Jirka, G. H. (1987b, 113(10)). Two-layer model of saline wedge. II: Predictions of mean properties. *ASCE J. Hydraul. Engng.*, pp. 1249-1263.

Armi, L. (1986, 163). The hydraulics of two flowing layers of different densities. *J. Fluid Mech.*, pp. 27-58.

Csanady, G. T. (1984, 14). Circulation induced by river inflow in well mixed water over a sloping continental shelf. *J. Phys. Oceanogr.*, pp. 1703-1711.

Cuthbertson, A., Laanearu, J., Wahlin, A., & Davies, P. (2011). Experimental and analytical investigation of dense gravity currents in a rotating, up-sloping and converging channel. *In press, Dynamics of Atmospheres and Oceans.* DOI:10.1016/j.dynatmoce.2011.09.001

Cuthbertson, A. J. S., Laanearu, J., & Davies, P. A. (2006, 6, 2(19)). Buoyancy-driven two-layer exchange flows across a slowly submerging barrier. *Environ. Fluid Mech.*, pp. 133-151.

Cuthbertson, A. J. S., Davies, P. A., Coates, M. J., & Guo, Y. (2004, 4). A modelling study of transient, buoyancy-driven exchange flow over a descending barrier. *Environ. Fluid Mech.*, pp. 127-155.

Davies, P. A. (2006). *Mixing and dispersion in stably stratified flows*. The Institute of Mathematics & Its Application Conference Series Number 68. Oxford University Press, Oxford, U.K.

Ivey, G. N., & Imberger, J. (1991, 21). On the nature of turbulence in a stratified fluid. Part I: the energetics of mixing. *J. Phys. Oceanogr.*, pp. 650-658.

Laanearu, J., & Davies, P. (2007, 45(1)). Hydraulic control of two-layer flow in "quadratic"-type channels. *IAHR J. Hydr. Res.*, pp. 3-12.

Laanearu, J., Vassiljev, A., & Davies, P. A. (2011a, 164(EM1)). Hydraulic modelling of stratified bi-directional flow in a river mouth. *IOC Engineering and Computational Mechanics*, pp. 207-216.

Laanearu, J., Cuthbertson, A., & Davies, P. (2011b). Dense-water overflow in a converging and up-sloping channel. *In: Proceedings of VII International Symposium of Stratified Flows: ISSF2011, Sapienza Universita Di Roma. Eds. Antonio Cenedese, Stefania Espa, Roperto Punini*, 8 pp.

Sargent, F. H. & Jirka, G. H. (1987, 113(10)). Experiments on the saline wedge. *ASCE J. Hydraul. Engng.*, pp. 1307-1324.

Pratt, L. J., & Whitehead, J. A. (2007). *Rotating Hydraulics: Nonlinear Topographic Effects in the Ocean and Atmosphere*. Springer Science + Business Media, LLC, New York, U.S.A.

Zhu, D. Z., & Lawrence, G. A. (2000, 126(12)). Hydraulics of exchange flows. *ASCE J. Hydraul. Engng.*, pp. 921-928.